Analytical model for estimation of digging forces and specific energy of cable shovel

M. Stavropoulou[*1] , G. Xiroudakis[2] and G. Exadaktylos[2]

[1]*Department of Dynamic, Tectonic and Applied Geology, Faculty of Geology and Geoenvironment, University of Athens, GR-15784, Greece*
[2]*Mining Engineering Design Laboratory, Department of Mineral Resources Engineering, Technical University of Crete, GR-73100 Chania, Greece*

(Received June 10, 2012, Revised March 5, 2013, Accepted March 6, 2013)

Abstract. An analytical algorithm for the estimation of the resistance forces exerted on the dipper of a cable shovel and the specific energy consumed in the cutting-loading process is presented. Forces due to payload and to cutting of geomaterials under given initial conditions, cutting trajectory of the bucket, bucket's design, and geomaterial properties are analytically computed. The excavation process has been modeled by means of a kinematical shovel model, as well as of dynamic payload and cutting resistance models. For the calculation of the cutting forces, a logsandwich passive failure mechanism of the geomaterial is considered, as has been found by considering that a slip surface propagates like a mixed mode crack. Subsequently, the Upper-Bound theorem of Limit Analysis Theory is applied for the approximate calculation of the maximum reacting forces exerted on the dipper of the cable shovel. This algorithm has been implemented into an Excel™ spreadsheet to facilitate user-friendly, "transparent" calculations and built-in data analysis techniques. Its use is demonstrated with a realistic application of a medium-sized shovel. It was found, among others, that the specific energy of cutting exhibits a size effect, such that it decreases as the (-1)-power of the cutting depth for the considered example application.

Keywords: ground-tool interaction;cable shovel; passive earth theory; limit analysis; fracture mechanics; cutting force; specific energy

1. Introduction

Cable shovels are widely used in casting ripped or blasted rock, in excavating soils, and in large-scale surface and stripping coal or oil sands operations, and other operations as well, due to their longevity, high productivity and their ability to exert high break-out forces. The shovel-truck mechanized method in surface excavations is flexible, efficient and it can be easily adjusted to different operating environments. The efficiency and costs of these operations greatly depend on the efficient use of the capital-intensive shovel excavators. However, the shovel-truck excavation method may become inefficient due to operating, environmental, and operator constraints. For example, data from eight surface mines show that loading costs range from 3% to 35% of operating costs with a mean of 15% (Hustrulid and Kuchta 1995). Operator preferences and

∗Corresponding author, Assistant Professor, E-mail: mstavrop@geol.uoa.gr

practices can lead to inefficiency leading to increased downtimes and lower productivity. Paraszczak *et al.* (2000) proposed real-time or near real-time machine performance measurements in order to mitigate the limitations of availability and utilization.

Hadjigeorgiou and Scoble (1988) critically discussed the optimization of excavation equipment selection regarding shovels and draglines, and performance evaluation, for different surface mine ground conditions in surface mines. They have asserted that the conventional use of materials classification schemes, based on empirical knowledge, can provide an immediate tool to mine operators. They have also recommended that this knowledge can be combined with other computerized methods of operations research to ensure increased productivity and equipment optimization. Most importantly they have commented that it is important to develop more elaborate theoretical and experimental studies on the actual mechanics of digging. These studies should provide "rational explanations" for digging performance, evaluated from practical experience, as well as data from machine performance monitoring. They have concluded that the benefit would be seen to arise from the ability to ensure that current excavating equipment be employed as productively as possible, whilst also assisting in the development of improved equipment design.

Shi and Joseph (2006) have pointed-out that the ground excavation model is the “heart” of the shovel’s model since most operating energy is consumed in this process. Such a model could then by used to predict the force distribution on the dipper resulting from the yielding and breaking of ground.

It should be noticed from the outset that there are many factors affecting the digging performance and the energy consumption of the various subsystems of the cable shovel, namely:

- the trajectory and capacity of the dipper (Maciejewski and Jarzebowski 2002), as well as the design of the dipper and the teeth attached to it (Shi and Joseph 2006),
- the cutting depth (Karpuz *et al*. 1992),
- the speed of the dipper depicted by the hoist and crowd velocities,
- the physical and mechanical properties of the geomaterials (i.e., jointed rock, soft rock, ripped or blasted rock, and soil) being excavated, such as particle (fragment) size distribution, particle shape and specific gravity, clay and moisture content, and ambient temperature (for example see discussion by Frimpong and Hu (2004) referring to excavation of oil sands by shovels),
- the repose angle of the bank, among others.

So, the development of an analytical comprehensive theoretical model for the realistic estimation of the cutting force that respects the geometry and trajectory of the dipper of the cable shovel, is indispensable for the optimization of cable shovel performance (Awuah-Offei and Frimpong 2007). In this context, the interaction between the working tools and the geomaterial has been extensively studied by many investigators. Blouin *et al.* (2001) have presented the most recent review of the work in this field. They have commented that the previous works are either theoretical or experimental approaches. The theoretical models are based on passive earth pressure theory. Most of the assumed tool-ground interaction theoretical models (e.g., Frimpong and Hu 2004, Awuah-Offei and Frimpong 2007, Lipsett and Moghaddam 2011, Awuah-Offei and Samuel Frimpong 2011 among many others) assume a planar failure mechanism (i.e., Coulomb-type) of the geomaterial in front of the cutting edge of the dipper, that may be considered approximate in most of the cases according to Chen (1975), and according to first principles of Mixed-Mode Fracture Mechanics (e.g., in Section 3 of this paper).

Herein a simple easy-to-use analytical algorithm for the quick calculation of the cable shovel forces required for excavating and loading of the material, for given initial conditions, material properties, and machine parameters and motions has been created and then has been implemented into an Excel™ spreadsheet. The innovative features of this study have as follows:

(a) The trajectory of the failure surface is found from simulations considering that the latter propagates as a mixed-mode crack; it was found that this shape is a log-spiral. Then the Upper-Bound theorem of Limit Analysis Theory for the passive log-spiral mechanism is applied for the calculation of the forces exerted on the dipper of the shovel.

(b) Hence, in this paper a non-planar failure surface inside the bank is considered in contrast to previous studies up-to-now.

(c) The kinematic and geomaterial cutting models have been implemented into an Excel™ spreadsheet in order to exploit the "transparency" of calculations obtained in this manner and to simplify as much as possible its use; this also emphasizes the fact that the whole model is analytical.

(d) It was found that the specific cutting energy exhibits a (-1) power relation with the cutting depth; this "size-effect" deserves more attention in the future, since it may be exploited for the optimization of the performance of a cable shovel.

The paper has the following structure: Section 2 presents the kinematical model of the cable shovel. Section 3 is devoted to the development of the geomaterial cutting model. Then, the analytical model that has been implemented into an Excel™ spreadsheet is illustrated in Section 4. Subsequently, a realistic example of a cable shovel performance is presented in Section 5. Finally, the main conclusions reached from this study are presented in Section 6.

2. Kinematics of cable shovel motion

The cable shovel is composed by three major assemblies, namely the lower and upper assemblies, and the attachment. The attachment assembly consists of the boom, the crowd mechanism, the dipper handle, and the dipper (Fig. 1). The shovel executes four primary motions, namely propelling, swinging, hoisting and crowding/retracting. The crowd/retract and hoist motions are achieved by the crowd and hoist motors, respectively. A brief description of each motion is as follows:

1. *Crowd*: Moving the crowd arm in and out from the boom (Fig.1)
2. *Hoist*: Moving the dipper and crowd arm up and down using the hoist ropes (Fig.1). Downward movement is by gravity as the hoist rope length is increased.
3. *Swing*: Rotation about the center of the machine's caterpillar tracks.
4. *Propel*: Movement of the entire machine via the caterpillar tracks.

The hoist machinery on the cable shovel consists of a rope drum that is rotated by the electric motor-driven hoist transmissions. The crowd motion refers to the motion of the dipper moving away from the centerline of the machine and towards the digging face. Digging is accomplished when the dipper is crowded (crowd extension) and hoisted up (hoist retraction) through the digging face along a trajectory depicted by these two independent motions, as well as by the starting position of the dipper.

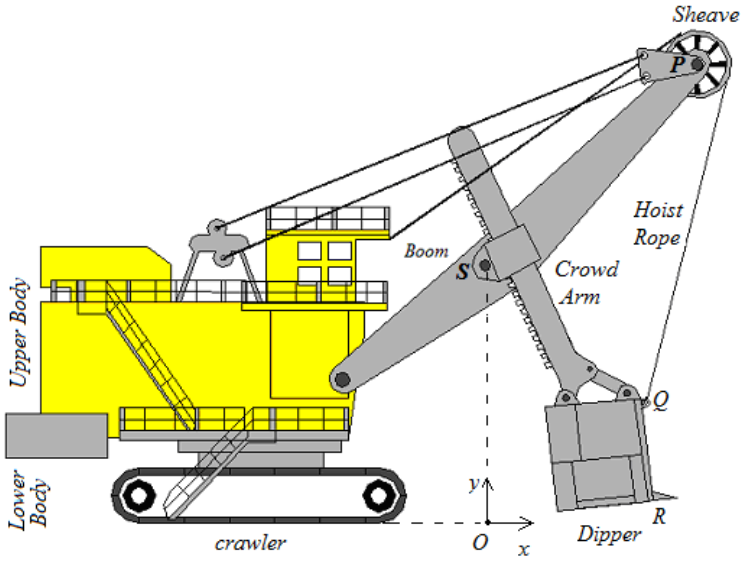

Fig. 1 Cable shovel nomenclature

A complete digging phase involves the digging tool (dipper) to the bank, filling it and then raising it clear to the bank. Fig. 2 shows a typical shovel dipper trajectory. As it is shown in this figure the shovel normally cleans loose material from the start-up (A) to the bench toe (B). Subsequently, the shovel dipper teeth engage the formation from B until excavation ends at the beginning of the coasting phase (C). During the final coasting phase (C–D) the dipper just moves to clear the bank.

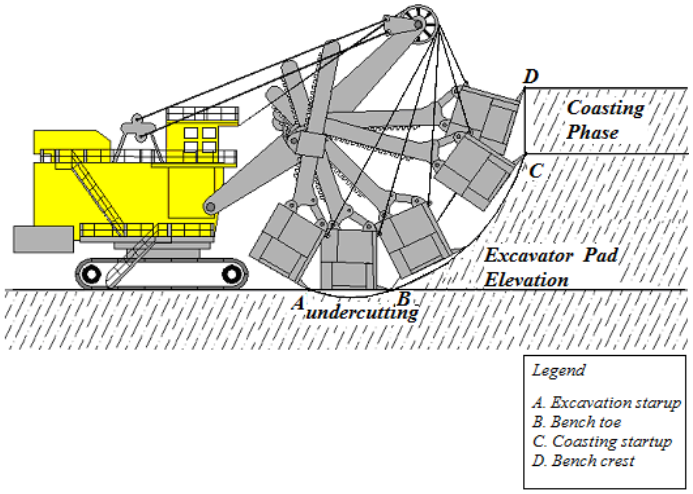

Fig. 2 The three distinct digging phases performed by a cable shovel

Hereafter, we consider only the planar motion of the dipper in the vertical plane as it moves through the bank (e.g., Fig. 2). More specifically, we consider a two-degrees of freedom (dof) model, namely by varying the length r_4 of the crowd arm with a prescribed velocity u_c and the length of the hoisting rope r_3 with a prescribed velocity u_h, as is shown in Fig. 3(a) while keeping always a constant boom length r_1, and in a first approximation considering sheave radius equal to zero, i.e., $r_2 \approx 0$. The geometry of this two d.o.f. model is depicted in Fig. 3(b).

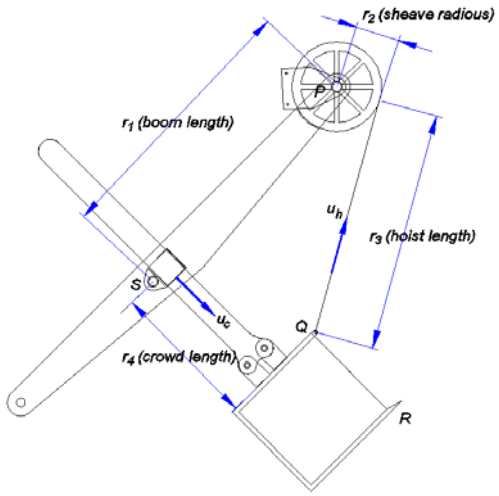

(a)

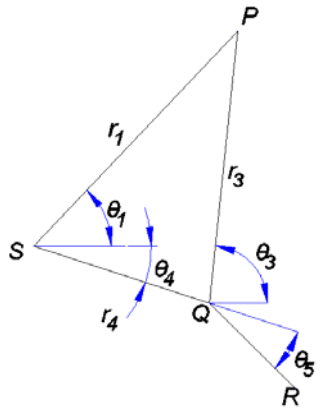

(b)

Fig. 3 Rope shovel degrees of freedom for digging: (a) variable crowd velocity u_c and variable hoist rope velocity u_h with positive directions of u_c and u_h as is shown in the figure and (b) two dof kinematical model of the excavation system (right). The attachment point of bucket is denoted by Q whereas the bucket teeth tip is denoted by R

The various length dimensions of the cable shovel at each time step during the digging cycle are found from: a) their respective values at the previous time step, and b) the hoist rope and crowd velocities by virtue of the following relations

$$\begin{aligned} r_1^{(i)} &= r_1^{(i-1)} \\ r_2^{(i)} &\approx 0 \\ r_3^{(i)} &= r_3^{(i-1)} - \dot{r}_3^{(i-1)}\delta t \\ r_4^{(i)} &= r_4^{(i-1)} + \dot{r}_4^{(i-1)}\delta t \\ \dot{r}_3^{(i-1)} &= u_h, \\ \dot{r}_4^{(i-1)} &= u_c \end{aligned} \tag{1}$$

wherein the superscript enclosed in a parenthesis is a positive integer indicating the number of time steps elapsed between the initial and current configuration, the dot over a symbol indicates differentiation with respect to time and δt is the constant time increment. The inclination of the boom θ_1 (e.g., Fig. 3(b)) is kept constant and is given as an input. The inclination of the hoist rope θ_3 measured anticlockwise, and of the angle θ_4 subtended between the crowd arm and the horizontal (e.g., Fig. 3(b)) that is measured clockwise, are found at each time step from the application of sine and cosine rules on the triangle PQS, respectively

$$\frac{r_1}{\sin(\pi - \theta_3 - \theta_4)} = \frac{r_3}{\sin(\theta_1 + \theta_4)} = \frac{r_4}{\sin(\theta_3 - \theta_1)} \tag{2}$$

$$r_3^2 = r_1^2 + r_4^2 - 2r_1\, r_4\, \cos(\theta_1 + \theta_4) \tag{3}$$

wherein the superscripts in parentheses have been omitted for simplicity.

Two models for the estimation of the respective most significant resistant forces exerted on a shovel dipper listed by Hemami *et al*. (1994), are presented in the next sections of this paper. Namely, the force required to overcome the weight of the loaded material in the bucket which is applied in center of mass of dipper payload O_1 (i.e., Fig. 4(a)), and the resistance to indentation and cutting acting at the tip of the bucket. The location of the point O_1 of the application of the force to overcome the weight, referred to a fixed Cartesian Oxy coordinate system, is also important for this purpose. The material distribution model illustrated in Figs. 4(a) and (b) was assumed for this purpose. These figures show the progressive filling of the bucket with loosened material in front of the bucket. The distribution is based on the fact that material once reaching its yield condition along certain slip lines will flow from the failure plane over the cutting lip to fill the bucket. This model allows the material cross-section at each time step to be approximated as a polygon. The vertices of the polygon that encloses the loaded loose material are calculated from the soil failure mechanism and the dipper geometry. In Fig. 4(a), ℓ indicates the depth of the side plate inside the soil bank, α_c refers to the cutting angle of teeth of the bucket, and β denotes the angle of the bank.

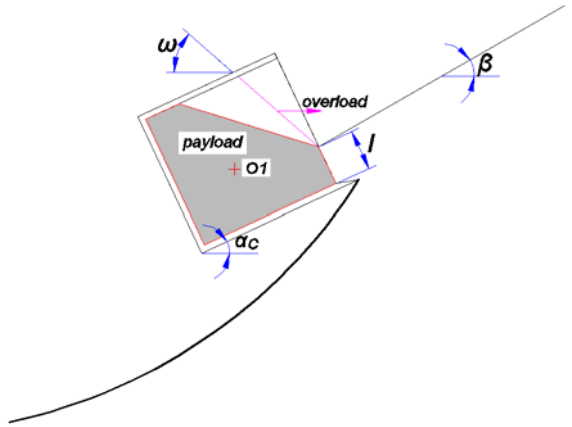

(a)

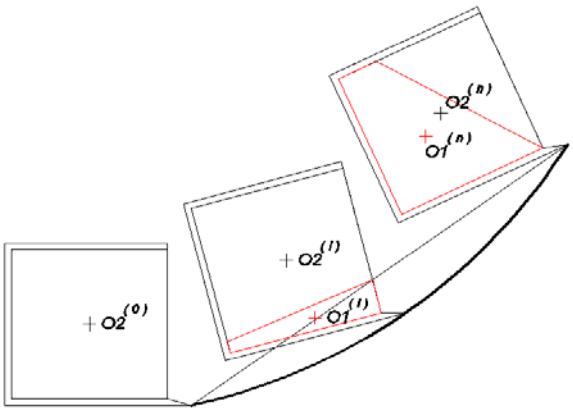

Legend
O1: Center of mass of shovel dipper payload
O2: Center of mass of shovel dipper bucket
β: slope angle
ω: max repose angle
αc: attack angle
l: bucket-rock contact length

(b)

Fig. 4 (a) Material distribution model and (b) filling process of the dipper during excavation

As is shown in Fig. 5, based on basic geometry principles, the cutting angle α_c is found at each time step to be given by the following relationship

$$\alpha_c + v + \theta_4 + \theta_5 = \pi \tag{4}$$

wherein v pertains to the bucket internal angle (Fig. 5), and θ_5 is the angle subtended between the base of the bucket and the crowd arm (e.g., Figs. 3(b) and 5).

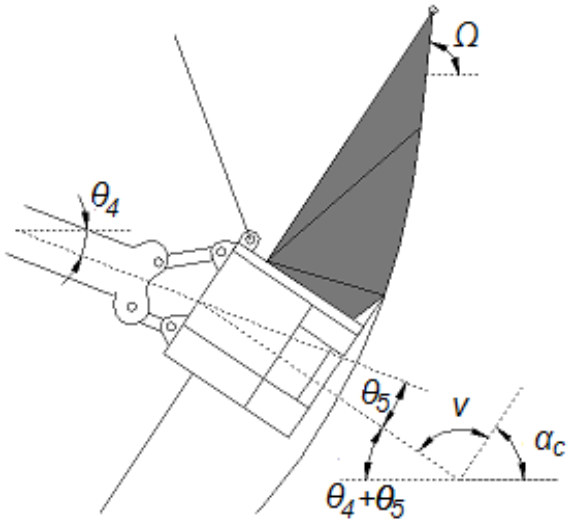

Fig. 5 Calculation of the cutting angle

3. Geomaterial cutting model

3.1 Crack trajectory inside the muckpile

For the creation of a reliable soil cutting model, the first step is to search for a realistic path for the propagating slip surface inside the muckpile, due to the penetration of the teeth of the dipper into it. For this purpose, we rely on first principles of Linear Elastic Fracture Mechanics (LEFM) viewing the thin discontinuity surface propagation inside the material as a classical mixed-mode crack propagation problem; it may be remarked here that the modeling of growth of slip surfaces in soils by virtue of Fracture Mechanics has been also done by Palmer and Rice (1973). Hence, it is assumed that there exists an initial crack occupying the line segment AB that is perpendicular to the inclined bucket's leading (cutting) edge inside the bank, EA, as is shown in Fig. 6. Quasistatic crack propagation was simulated by the code G2TWODD (i.e., acronym for Grade-2 Two-Dimensional Displacement Discontinuity) that is dedicated for fast and accurate calculations of Stress Intensity Factors (SIFs), as well as of displacements and stresses in cracked elastic bodies (Exadaktylos and Xiroudakis 2009, 2010a and 2010b). The initial crack occupying the line segment AB was discretized with ten tractionless linear displacement discontinuity elements of equal size. This number of elements has been found to be adequate for our purposes based on the repeatability of computed results by using more elements. The rigid wall EA in Fig. 6 was discretized with eighteen elements with the same size of the crack elements (since G2TWODD method requires elements of equal size) subjected to constant and equal normal and tangential tractions $\sigma_n = \sigma_s$, respectively, that are large enough to maintain continuous crack growth up to the free surface of the bank. The free surface ED (Fig. 6) was discretized with boundary elements that were free of traction. Mode I and II SIF's, K_I, K_{II}, respectively, were calculated after each crack increment. The crack propagation increment had always the size of the initial crack element size.

The fracture propagation criterion was based on the maximum local circumferential (hoop) tensile stress $\sigma_{\theta\theta}$ which is given by the following formula (Parker 1981)

$$\sigma_{\theta\theta}(r,\theta)=\frac{K_{\theta\theta}(\theta)}{\sqrt{2\pi r}}+o\left(\sqrt{r}\right) \tag{5}$$

where $o(\cdot)$ denotes Landau's order-of-magnitude symbol, and $K_{\theta\theta}$ is the effective stress intensity factor given as follows

$$K_{\theta\theta}(\theta)=\cos^2\left(\frac{\theta}{2}\right)\left(K_I\cos\left(\frac{\theta}{2}\right)-3K_{II}\sin\left(\frac{\theta}{2}\right)\right) \tag{6}$$

and r,θ denote the pair of radial and tangential polar coordinates, respectively, with centre at the crack tip. The crack growth occurs along the direction that $K_{\theta\theta}$ reaches the critical value of mode I SIF denoted by the symbol K_{Ic}, as it is depicted by the following relation

$$\max_{\theta}\left\{K_{\theta\theta}(\theta)\right\}=K_{Ic} \tag{7}$$

The direction of propagation defined as the angle which maximizes the effective stress intensity factor and is expressed as a function of the ratio K_I/K_{II}

$$\theta_p=2\arctan\left(\frac{1}{4}\frac{K_I}{K_{II}}\pm\frac{1}{4}\sqrt{\left(\frac{K_I}{K_{II}}\right)^2+8}\right) \tag{8}$$

Eq. (8) can be used to rewrite the condition expressed by Eq. (6) of crack extension into the soil bank

$$4\sqrt{2}\left|K_{II}\right|\frac{\left(\frac{K_I}{K_{II}}+3\sqrt{\left(\frac{K_I}{K_{II}}\right)^2+8}\right)}{\left\{\left(\frac{K_I}{K_{II}}\right)^2+12-\left(\frac{K_I}{K_{II}}\right)\sqrt{\left(\frac{K_I}{K_{II}}\right)^2+8}\right\}^{\frac{3}{2}}}=K_{Ic} \tag{9}$$

The use of the maximum local tensile stress criterion is justified since it has been demonstrated by virtue of discrete element modeling (Stavropoulou 2006) that during the cutting process, tensile forces are exerted locally on the particles along the potential crack trajectory.

By virtue of the above fracture criterion a quasi-static crack growth simulation may be subsequently performed for the prediction of the crack path. For this purpose a step by step process is followed. We consider a constant crack length increment Δa, which is the distance

between two consecutive locations in time of the crack tip. Once Δa has been chosen, the algorithm has as follows:

1. give the initial crack tip coordinates $x_{tip}^{(i)}$ for the initial configuration ($i = 0$);
2. proceed with the next simulation time step ($i+1$);
3. compute the values of the stress intensity factors, K_I and K_{II} at the crack tip;
4. determine the angle of propagation θ_p using Eq. (8);
5. update the crack tip coordinates $x_{tip}^{(i+1)} = x_{tip}^{(i)} + \Delta a \cdot \left[\cos(\theta_p), \sin(\theta_p)\right]$;
6. return to the step 2 of the algorithm;
7. continue until the crack tip reaches the free surface of the bank.

From several simulations it was found that the crack follows a logarithmic spiral (logspiral) path BC and afterwards continues along a linear segment CD as is illustrated in Fig. 6. In the same figure it may be observed that the center O of the polar coordinates (ρ, ϑ) of the logspiral crack segment lies at a small distance above the muckpile and is described with the following equation,

$$\rho = 3.15 \exp(0.325\vartheta) \tag{9a}$$

for the particular initial crack, loading and geometry configurations.

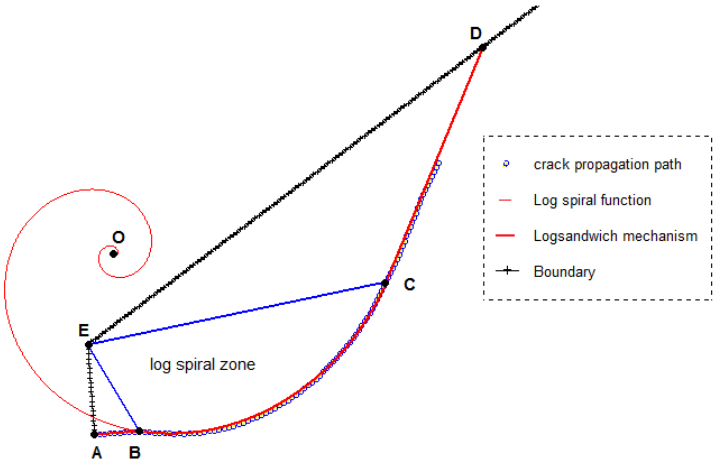

Fig. 6 Crack trajectory (dotted line) resembling a listric normal fault. On this crack trajectory the logspiral curve OBC and the line CD are superimposed with continuous lines

3.2 Analytical muckpile cutting model

According to the above preliminary analysis, the muckpile cutting process with the shovel dipper is modeled by a logsandwich kinematical failure mechanism, as is displayed in Figs. 7(a) and (b), and then the limit analysis kinematical method for rigid perfectly plastic geomaterials is

applied. The slip lines separating the rigid regions of the mechanism are modeled as stationary velocity discontinuity lines. This failure mechanism may be described as follows:

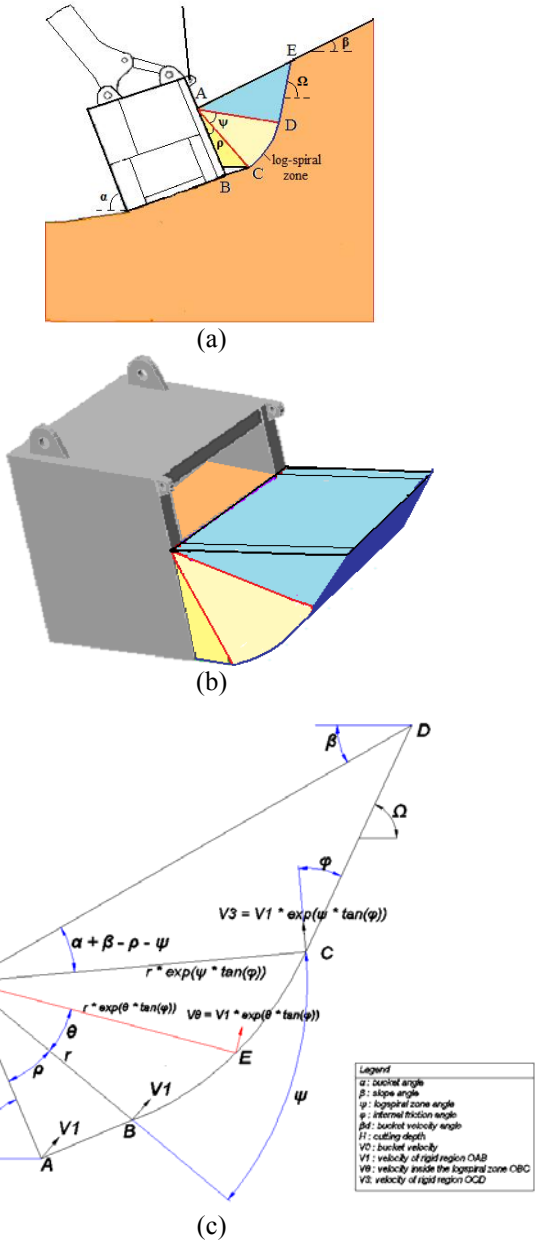

Fig. 7 Soil cutting mechanism: (a) the two triangle mechanism projected on the vertical plane normal to the blade of the dipper and (b) perspective view of the three failure planes inside the soil bank

1) The first rigid triangle ABC (Fig. 7(a)) is formed from the trace BC of the teeth on the vertical plane, the trace AC of the shear localization plane extending from the tip of the teeth at point C to the free surface at point A that is the intersection of the side plate of the bucket with the free surface, and the trace AB that represents the dipper's leading (cutting) edge inside the bank. If the length ℓ of the side plate of the bucket inside the bank, and the length ℓ_t of the bucket's teeth are known, then the angle ρ subtended between the side plate and the failure plane with trace AC is also known.

2) The second region ACD is a logarithmic spiral slip line sandwiched between two rigid triangles ABC and ADE.

3) The second triangle ADE, is formed from the traces AD and AE and a third trace DE that is a shear band making an angle Ω with the horizontal.

Discontinuities AC and AD are necessary for the accommodation of the continuous deformation after the full development of the other three shear bands, namely BC developed in a first phase as well as CD and DE, developed in the second and third stages, respectively. The final fully developed kinematical failure mechanism is also illustrated in Fig. 7(b). It is worth mentioning that the work expended for the penetration of the teeth into the bank of the soil is taken into account in this model by the presence of the slip line BC.

Three angles are needed to describe the full failure mechanism, that is the angles ρ, ψ and Ω for given slope angle of the bank β, and bucket's alignment angle α (e.g. Fig. 7(a)). As it was mentioned above, the initially formed failure plane BC is parallel to bucket teeth and has a length equal to the length of teeth. Hence, the first angle may be easily found in the following manner

$$\rho = \tan^{-1}\left(\frac{\ell_t}{\ell}\right) \tag{10}$$

If the velocities for the two rigid triangles are assumed to be perpendicular to the radial lines AC and AD (or to the lines OB and OC in Fig. 7(c)), then only two angular parameters ρ and ψ describe the mechanism completely. It is noted here that from elementary geometry it can be found that the third angle Ω is given by the relationship

$$\Omega = \frac{\pi}{2} - \phi - \alpha + \rho + \psi \tag{11}$$

Hence, the only remaining unknown angle ψ may be found by the minimization of the resultant passive pressure required to create the assumed failure mechanism inside a Mohr-Coulomb material following the associated flow rule and characterized by unit weight γ, cohesion c and internal friction angle ϕ. In the framework of the passive earth pressure theory, the total passive specific pressure Pp applied to the shovel dipper with zero surcharge load may be expressed in a concise manner as follows (Chen 1975)

$$Pp = \frac{1}{2} K_{p\gamma} \gamma h^2 + K_{pc} c h, \quad h = \ell \sin\alpha \tag{12}$$

The dimensionless coefficients $K_{p\gamma}, K_{pc}$ for the logsandwich mechanism accounting for the weight and the cohesion of the soil, respectively, could be found by virtue of the upper-bound theorem of Limit Analysis Theory which is appropriate for prediction of excavation loads. This is achieved by equating the rate of external work performed by the dipper with the rate of internal work dissipated on the shear bands AC, BC, CD, AD and DE. The final results for the two cases of a smooth and rough tool (wall), respectively, may be found in Chen's textbook (Chen 1975); however, for clarity of the presentation, these expressions with some minor modifications referring to corrections of few misprints, as well as to the consideration of velocity of the wall at an arbitrary inclination β_d w.r.t. the horizontal (e.g., Fig. 7(c))re presented below:

(i) For the case of the smooth wall ($\delta < \phi$), where δ denotes the interfacial friction angle of the bucket-soil contact, we have

$$
\begin{aligned}
K_{p\gamma} = & \frac{\sec(\delta)}{\sin(\alpha-\beta_d)+\tan\delta\cos(\alpha-\beta_d)-\tan\delta\dfrac{\cos(\alpha-\rho-\beta_d)}{\cos\rho}}\frac{\sin(\alpha-\beta_d)}{\cos\rho}\times \\
& \times\left[\frac{\tan(\rho)\cos(\alpha-\rho)}{\sin^2\alpha}+\frac{1}{(9\tan^2\phi+1)\sin^2\alpha\cos^2\rho}\times\right. \\
& \times\{(3\tan\phi\cos(\alpha-\rho-\psi)-\sin(\alpha-\rho-\psi))\exp(3\theta\tan\phi)- \\
& -(3\tan\phi\cos(\alpha-\rho)+\sin(\alpha-\rho))\}+ \\
& \left.+\frac{\cos\phi\sin(\alpha+\beta-\rho-\psi)\cos(\alpha-\rho-\psi)}{\sin^2\alpha\cos^2\rho\cos(\alpha+\beta-\rho-\psi+\phi)}\exp(3\theta\tan\phi)\right],
\end{aligned}
\tag{13a}
$$

And

$$
\begin{aligned}
K_{pc} = & \frac{\sec\delta}{\sin(\alpha-\beta_d)+\tan\delta\cos(\alpha-\beta_d)-\tan\delta\dfrac{\cos(\alpha-\rho-\beta_d)}{\cos\rho}}\cdot\frac{\sin(\alpha-\beta_d)}{\cos\rho}\times \\
& \times\left[\frac{\sin\rho}{\sin\alpha}+\frac{1}{2}\frac{\cot\phi[\exp(2\theta\tan\phi)-1]}{\sin\alpha\cos\rho}+\frac{\sin(\alpha+\beta-\rho-\psi)\cos\phi\exp(2\theta\tan\phi)}{\sin\alpha\cos\rho\cos(\alpha+\beta-\rho-\psi+\phi)}\right]
\end{aligned}
\tag{13b}
$$

(ii) For the case of a rough wall ($\delta \geq \phi$), we have

$$
\begin{aligned}
K_{p\gamma} = & \frac{\sec\delta}{\sin(\alpha-\beta_d)+\tan\delta\cos(\alpha-\beta_d)}\frac{\sin(\alpha-\beta_d+\phi)}{\cos(\rho+\phi)}\times \\
& \times\left[\frac{\tan\rho\cos(\alpha-\rho)}{\sin^2\alpha}+\frac{1}{(9\tan^2\phi+1)\sin^2\alpha\cos^2\rho}\times\right. \\
& \times\{(3\tan\phi\cos(\alpha-\rho-\psi)-\sin(\alpha-\rho-\psi))\exp(3\theta\tan\phi)- \\
& -(3\tan\phi\cos(\alpha-\rho)+\sin(\alpha-\rho))\}+ \\
& \left.+\frac{\cos\phi\sin(\alpha+\beta-\rho-\psi)\cos(\alpha-\rho-\psi)}{\sin^2\alpha\cos^2\rho\cos(\alpha+\beta-\rho-\psi+\phi)}\exp(3\theta\tan\phi)\right]
\end{aligned}
\tag{13c}
$$

and

$$
\begin{aligned}
K_{pc} = & \frac{\sec\delta}{\sin(\alpha-\beta_d)+\tan\delta\cos(\alpha-\beta_d)}\times \\
& \times\left[\frac{\cos\phi\cos(\alpha-\rho-\beta_d)}{\sin\alpha\cos(\rho+\phi)}+\frac{\sin(\alpha-\beta_d+\phi)}{\cos(\rho+\phi)}\cdot\left\{\frac{\sin\rho}{\sin\alpha}+\right.\right. \\
& \left.\left.+\frac{1}{2}\frac{\cot\phi[\exp(2\theta\tan\phi)-1]}{\sin\alpha\cos\rho}+\frac{\sin(\alpha+\beta-\rho-\psi)\cos\phi\exp(2\theta\tan(\phi))}{\sin\alpha\cos\rho\cos(\alpha+\beta-\rho-\psi+\phi)}\right\}\right]
\end{aligned}
\tag{13d}
$$

The remaining unknown angle ψ of the log-spiral zone that varies in the range $0 \le \psi \le \alpha+\beta-\rho$ could be found by requiring the minimization of the resultant passive pressure P_p as is given by Eqs. (12) ÷ (13). It was found that the optimum angle ψ almost coincides with the maximum value which means that the triangle ADE in Fig. 7(a) is very small and it could be discarded; therefore, for either smooth or rough wall conditions this angle may be approximated as follows

$$\psi \approx \alpha+\beta-\rho \tag{14}$$

Finally, the horizontal and vertical components of the passive specific earth pressure denoted by P and Q, respectively, are given by

$$
\begin{aligned}
P &= P_P\cos(\delta-\alpha_c), \\
Q &= P_P\sin(\delta-\alpha_c)
\end{aligned}
\tag{15}
$$

The respective horizontal and vertical components of the cutting force are then found by multiplying the above respective specific pressures with the total width of the teeth. It is worth noting that in this model the teeth wear that produces tool bluntness could be taken into account by appropriately increasing the total width of the teeth. Furthermore, the cutting forces of the side

plates are derived by multiplying the above specific pressures with the total thickness of the two side plates of the bucket.

It should be noted that the above solution is not limited only to drained conditions occuring for example in dry, coarse grained soils or loose jointed or blasted rocks. In fact Detournay and Atkinson (2000) explicitly showed that in the other limiting case of undrained behavior of the material under the following assumptions: (a) the material is shear-dilatant, (b) the shear strength across the failure surface depends on the effective normal stress, and (c) the pore pressure variation in the intact material is governed by the diffusion equation, then the calculated pressure drop is very large suggesting a cavitation in the shear zone (i.e., pore pressure in the shear failure zone practically vanishes). This means that the cutting forces and the specific energy of cutting are independent of the initial virgin pore pressure and the above formulae (12) ÷ (15) hold true also for the undrained case.

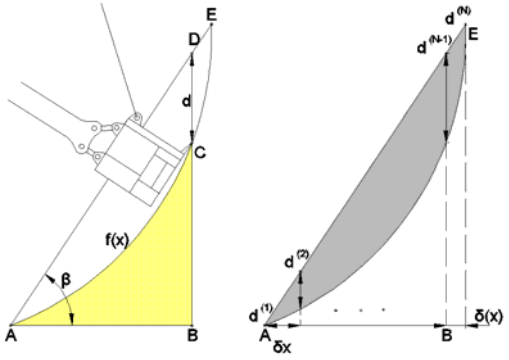

$$\mathrm{A}\left(x^{(0)}, y^{(0)}\right)$$
$$B\left(x^{(t-1)}, y^{(0)}\right)$$
$$C\left(x^{(t-1)}, \tan\beta \cdot \left(x^{(t-1)} - x^{(0)}\right) + y^{(0)} - d\right)$$
$$D\left(x^{(t-1)}, \tan\beta \cdot \left(x^{(t-1)} - x^{(0)}\right) + y^{(0)}\right)$$
$$E\left(x^{(t)}, \tan\beta \cdot \left(x^{(t)} - x^{(0)}\right) + y^{(0)}\right)$$

Fig. 8 Calculation of area of loose material inside the bucket at various time steps and coordinates of various points used in these calculations. The line segment CE denotes the next failure plane inside the bank

4. The analytical algorithm

4.1 The material weight submodel

The payload resistance model is based on the assumptions of material homogeneity and of negligible spillage of the material during loading. Furthermore, the calculations are performed in a first phase considering a plane model, whereas the dipper width w and the total width of the teeth needed for the calculation of the payload and cutting force, respectively, are incorporated at a

latter stage. Also, the failure plane in the material whose trace on the vertical plane is designated as CE in Fig. 8, is assumed to be curvilinear, as was also mentioned in the preceding section referring to the logsandwich kinematical failure mechanism.

At each time increment the total payload transported by the dipper is contained in the area swept by the dipper up to the current failure plane. This is the area of the triangle ABD plus the area of the curvilinear triangle CDE minus the area of the curvilinear triangle ABC defined by the trajectory $y = f(x)$ travelled by the dipper. Then, the product of this area with the dipper width w is the volume of the loaded material inside the bucket. Referring to Fig. 8, the desired cross-sectional area, A_c of the payload, is given by the following relation

$$\begin{aligned} A_c &= E_{ACE} = E_{ABD} + E_{CDE} - E_{ABC} \approx \\ &\approx \frac{1}{2}(x_t - x_0)y_D + \frac{1}{2}(x_E - x_t)d - \left(\int_{x_o}^{x_t} f(x)dx - (x_t - x_0)y_0 \right) \end{aligned} \tag{16}$$

wherein x denotes the abscissa of the dipper's tip trajectory referred to a fixed Cartesian coordinate system, the subscripts "*0*", "*t*" and "E" denote the starting position, an intermediate position at time t and the abscissa of point E, whereas y_D denotes the ordinate of point D and d the cutting depth in Fig. 8.

The integral appearing in the above expression (16) may be estimated numerically once the coordinates of the points on the trajectory $f(x)$ of the dipper are known. The latter could be found at the k^{th} time step that lies between 2 and N, where N designates the total number of time steps of a digging cycle, as follows

$$\begin{aligned} A_c^{(k)} &\approx \frac{1}{2}\sum_{i=2}^{k}\left(\left(d^{(i)} + d^{(i-1)}\right)\delta x + \frac{\left(d^{(i)}\right)^2}{\tan\Omega^{(i)} - \tan\beta} - \frac{\left(d^{(i-1)}\right)^2}{\tan\Omega^{(i-1)} - \tan\beta} \right), \\ \Omega^{(i)}=\Omega^{(i-1)} \Rightarrow \quad A_c^{(k)} &\approx \frac{1}{2}\sum_{i=2}^{k}\left(\left(d^{(i)} + d^{(i-1)}\right)\delta x \right), \quad 2 \le k \le N \end{aligned} \tag{17}$$

The weight F_1 of the material in the dipper is thus given by the following relationship

$$F_1 = A_c w \gamma \tag{18}$$

where γ denotes the unit weight of the loose material.

As it was presented in Figs. 4(a) and (b) the crosssectional shape of dipper's payload could be approximated with a polygon. The Cartesian coordinates (x, y) of the center of mass O_1 of the loose material inside the dipper could be found by dividing the polygon into n elementary geometrical shapes (i.e., triangles or rectangles) with known center of masses and then applying the following relationship

$$O_1\left(\frac{\iint x dxdy}{\iint dxdy}, \frac{\iint y dxdy}{\iint dxdy}\right) \approx O_1\left(\frac{\sum_{i=1}^{n} x_c^{(i)} A^{(i)}}{\sum_{i=1}^{n} A^{(i)}}, \frac{\sum_{i=1}^{n} y_c^{(i)} A^{(i)}}{\sum_{i=1}^{n} A^{(i)}}\right) \tag{19}$$

where $x_c^{(i)}, y_c^{(i)}, A^{(i)}$ are the coordinates of center of mass and the area of the simple shape $i\,(i=1,...,n)$, respectively. The same algorithm can be applied for the determination of the dynamic coordinates of the centroid of the dipper O_2 (e.g., Fig. 4(b)) which is the point of application of the force required to move the empty bucket.

The algorithm for the dynamic material weight subsystem is presented in the flowchart of Fig. 9 in which N indicates the final number of time steps, and t stands for the number of the time steps. The bucket capacity is specified as an input value. The initial cross-sectional area A_{c0} for $t=0$ is set equal to zero. Null is also the incremental cross-sectional area of the payload either when the bucket capacity is reached or the bucket is outside the bank (e.g., for $d_1 \le 0$ according to the notation of Fig. 10).

4.2 The material cutting submodel

The only difficulty in this model is the determination of the penetration length ℓ, of the side plates of the dipper inside the bank. In order to determine this length the cutting depths d_1 and d_2 as they are defined in Fig's 10 a÷e should be first determined. When the dipper's tip (point R) is in the bank, but the point of attachment (point Q) is not (Fig. 10(b)), the length ℓ is given in Fig. 10c. Apart from this case, there are three other distinct possibilities: (i) the dipper tip is just touching the bank surface (Fig. 10(a)); (ii) both of the dipper's tip and the point of attachment is completely out of the bank (Fig. 10(e)), and (iii) both the tip and the point of attachment are inside the bank (Fig. 10(d)). In the first two cases, the bucket side plates are not in the bank and thus ℓ is null. In the third case, the length ℓ, is equal to total side plate length QR. Finally, the algorithm employed for the calculation of ℓ at each time step is described in the flowchart in Fig. 11.

4.3 Specific energies of the crowd, hoist and cutting components of the shovel

In order to answer the question referring to which of the two motors of crowd or hoist is more important in performing useful work, we introduce the following definitions of specific energies referring to these two actions of the shovel, SE_C, SE_H, respectively.

$$SE_C = \frac{\int_0^t C\dot{r}_4 dt}{V}, \qquad SE_H = \frac{\int_0^t H\dot{r}_3 dt}{V} \tag{20}$$

where t denotes the current time, C, H denote the forces exerted on the crowd and hoist, respectively, as is illustrated in Fig. 12(a), and V is the current payload volume in the dipper. These forces may be found from the application of the static equilibrium equations on the free body diagram of the shovel, as is illustrated in Fig. 12(b) below. For a particular shovel, the hoist and crowd forces depend on the kinematics and the bank formation resistance, which in turn depends on the bank material properties.

The equilibrium equations along the horizontal Ox and vertical directions Oy, respectively, take the form

$$\begin{aligned} \sum F_x &= H\cos\theta_3 + C\cos\theta_4 - P = F_x = m\left(\ddot{r}_{3x} + \ddot{r}_{4x}\right) \\ \sum F_y &= H\sin\theta_3 - C\sin\theta_4 + Q = F_y = m\left(\ddot{r}_{3y} - \ddot{r}_{4y}\right) \end{aligned} \tag{21}$$

where $\ddot{r}_{3x}, \ddot{r}_{3y}, \ddot{r}_{4x}, \ddot{r}_{4y}$ denote the accelerations of hoist rope and crowd arm along the Ox- and Oy-directions, respectively, and are estimated from the following formulae

$$\begin{aligned} \ddot{r}_{3x}^{(i)} &= \frac{du_{hx}}{dt} = \frac{u_h\left(\cos\theta_3^{(i)} - \cos\theta_3^{(i-1)}\right)}{dt}, \\ \ddot{r}_{3y}^{(i)} &= \frac{du_{hy}}{dt} = \frac{u_h\left(\sin\theta_3^{(i)} - \sin\theta_3^{(i-1)}\right)}{dt}, \\ \ddot{r}_{4x}^{(i)} &= \frac{du_{cx}}{dt} = \frac{u_c\left(\cos\theta_4^{(i)} - \cos\theta_4^{(i-1)}\right)}{dt}, \\ \ddot{r}_{4y}^{(i)} &= \frac{du_{cy}}{dt} = \frac{u_c\left(\sin\theta_4^{(i)} - \sin\theta_4^{(i-1)}\right)}{dt} \end{aligned} \tag{22}$$

in which as was also previously noted, the superscript (i) enclosed in a parenthesis is a positive integer indicating the number of elapsed time steps corresponding to the current position of the dipper, as is illustrated in Fig. 12(c).

Also an important performance parameter depicting the cutting efficiency of the cable shovel is the specific energy of cutting, SE_c, which is herein defined in the following fashion

$$SE_c = \frac{\delta W_{wall}}{\delta V} = \frac{P_p V_0\left[\sin\left(\alpha - \beta_d\right) + \tan\delta\cos\left(\alpha - \beta_d\right)\right]\cos\delta}{\delta V}dt \tag{23}$$

where δW_{wall} is the incremental work expended in moving the wall of the bucket during the constant time step interval δt, δV the incremental amount of excavated volume, and V_0 is the current velocity of the bucket's leading (cutting) edge as is displayed in Fig. 7(c).

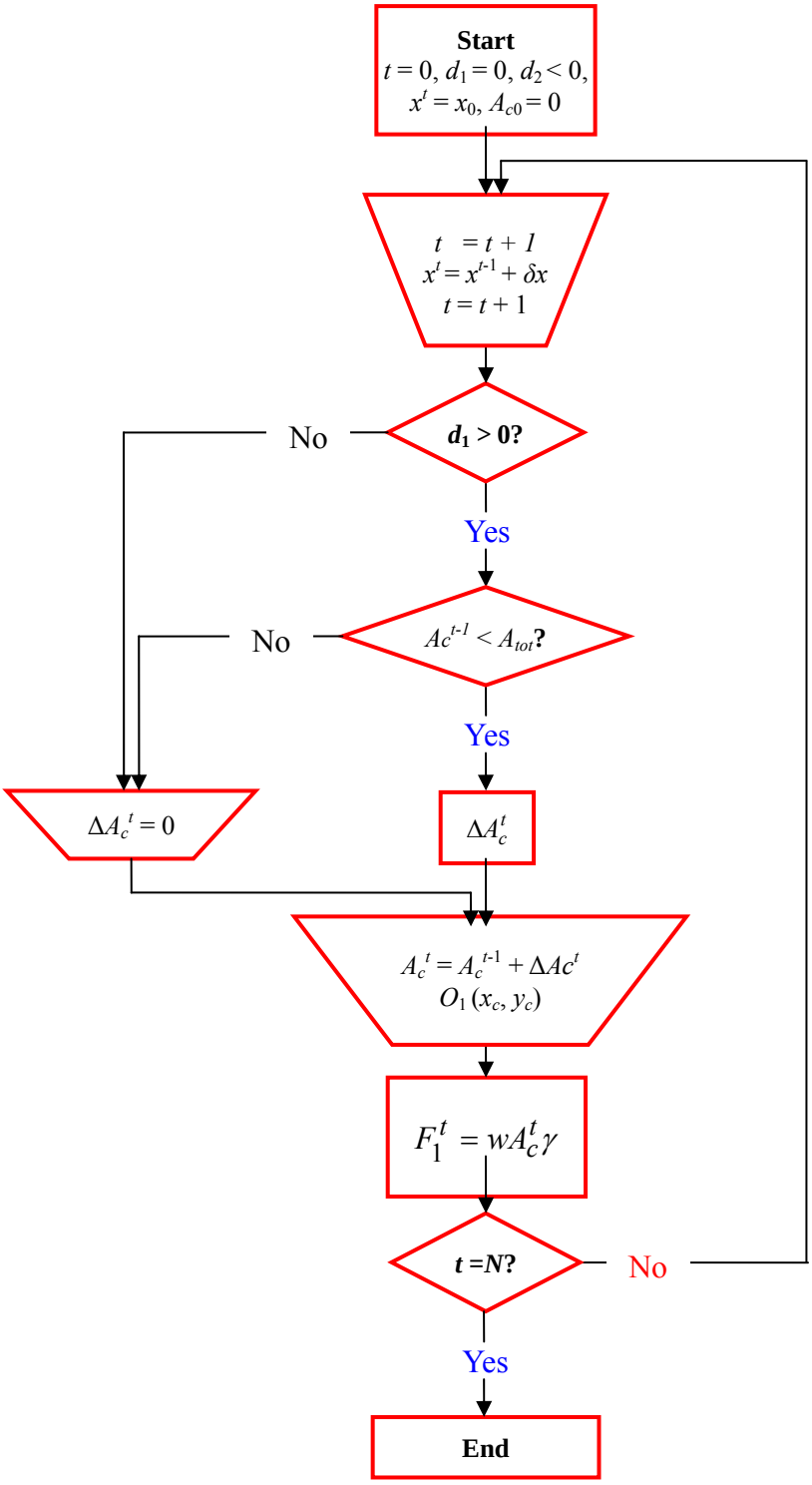

Fig. 9 Flowchart of the material weight model

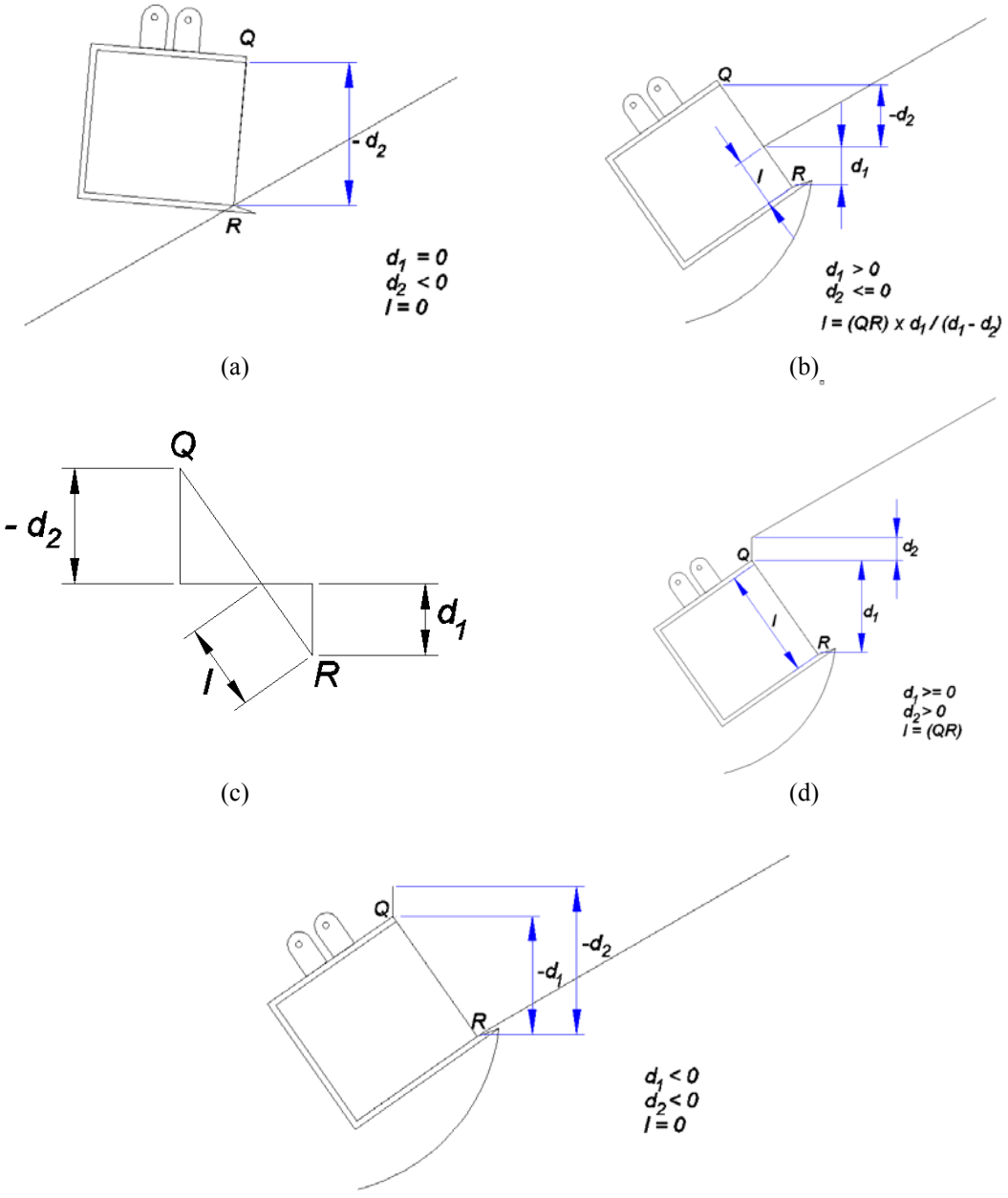

Fig. 10 Vertical sections of the four distinct cases for the calculation of the side length of the dipper inside the bank

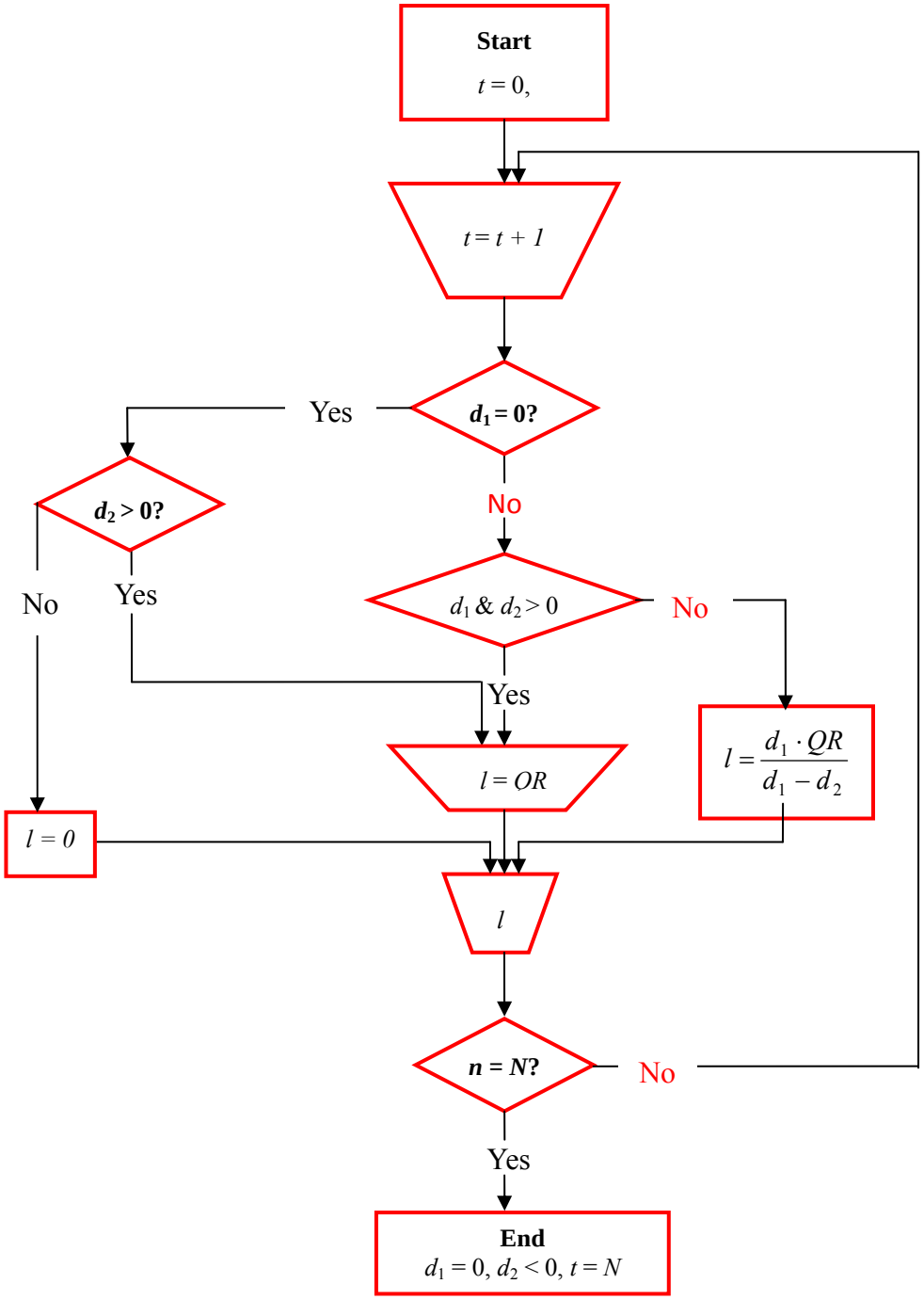

Fig. 11 Flowchart for the determination of side length of the bucket inside the bank

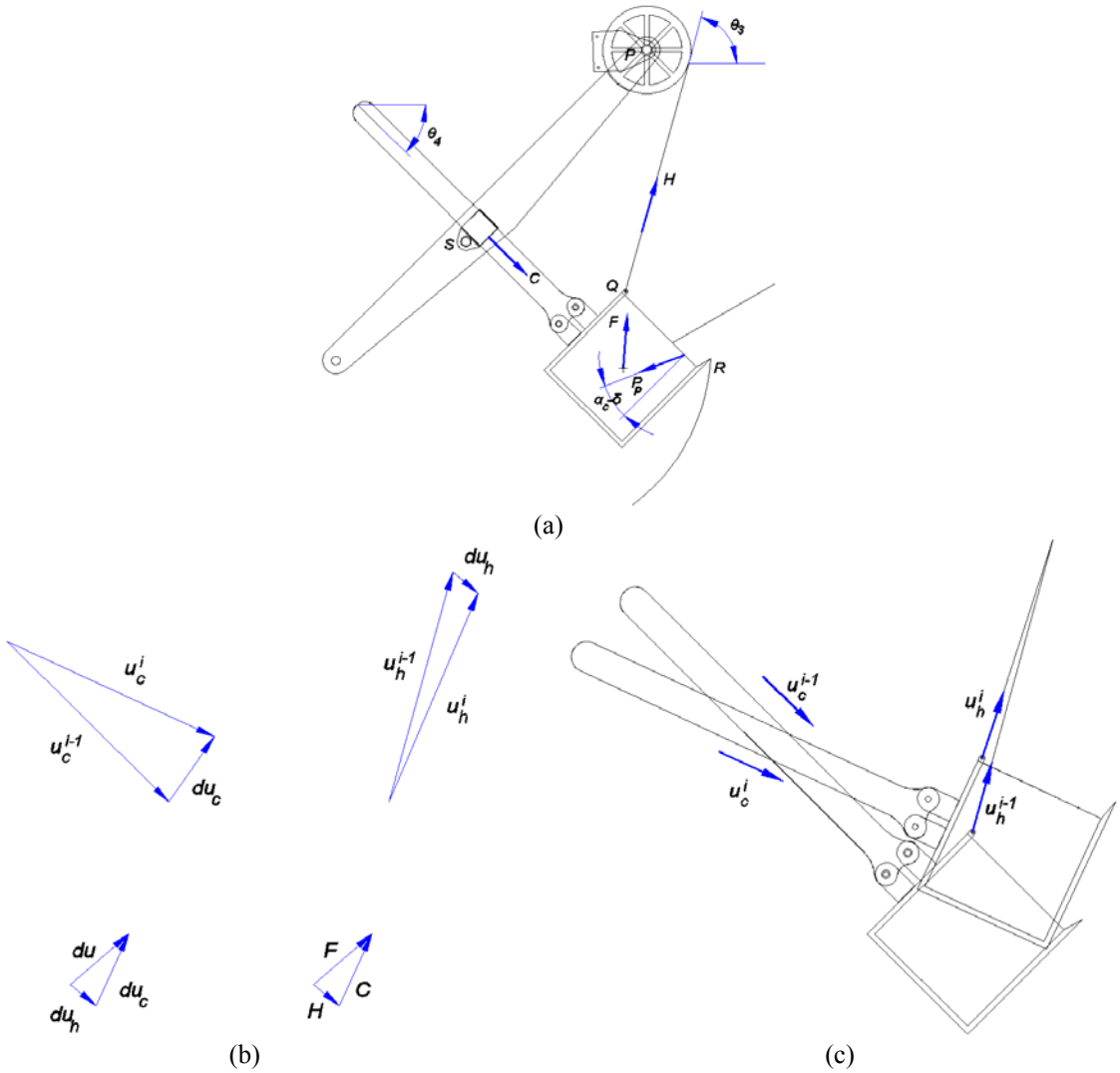

Fig. 12 (a) Crowd and hoist forces calculation, (b) velocity and force diagrams, and (c) crowd and hoist velocities at successive time increments

5. Example application

A medium-sized cable shovel is considered with a dipper capacity of 13 m^3 and other parameters as is shown in Table 1. For clarity of the example, Figs. 13(a) and (b) display the geometrical characteristics of the dipper. The initial values of the various parameters involved in the calculations are displayed in Table 2. These pertain to the initial coordinates of the points R and Q of the bucket as shown in Fig. 3(c), the initial cutting angle α_{c0}, as well as the lengths and inclinations of the boom, hoisting rope and crowd, respectively, also indicated in Fig. 3(c). Given

in addition the constant soil parameters indicated in Table 3, the payload and geomaterial cutting resistance forces among other significant parameters that affect these calculations (i.e., trajectory of the dipper, cutting angle etc), may be easily computed by virtue of the algorithm presented above.

Table 1 Values of the parameters of the shovel, the bank and the algorithm

Description of parameters	Value
Side plate length QR (see Fig. 3(c)) [m]	2.75
Dipper angle, ν [deg]	90
Dipper width, w [m]	2.74
Dipper length, L [m]	2.74
Dipper capacity, V [m^3]	13
Dipper fill factor [-]	1.1
Dipper weight [kN]	210
Side plate thickness, dw [m]	0.0127
Teeth length, ℓ_t [m]	0.1
Total width of teeth [m]	1.245
Time step, dt [sec]	0.03
Bank slope, β [deg]	60

Table 2 Initial values of the various kinematical parameters

Parameters	Values
XR_0 [m]	4.00
YR_0 [m]	0.00
XQ_0 [m]	4.00
YQ_0 [m]	2.75
α_{c0} [deg]	0
$r_1^{(0)}$ [m]	15.24
$r_3^{(0)}$ [m]	20.082
$r_4^{(0)}$ [m]	9.059
$\theta_1^{(0)}$ [deg]	45.00
$\theta_3^{(0)}$ [deg]	70.28
$\theta_4^{(0)}$ [deg]	63.8
$\theta_5^{(0)}$ [deg]	26.203

Table 3 Geomaterial parameters

Material Properties	Value
Soil-metal interfacial friction angle, δ [deg]	35
Soil unit weight, γ [kN/m^3]	15
Soil swelling factor	1.1
Soil internal friction angle, ϕ [deg]	32
Soil cohesion, c [kPa]	15

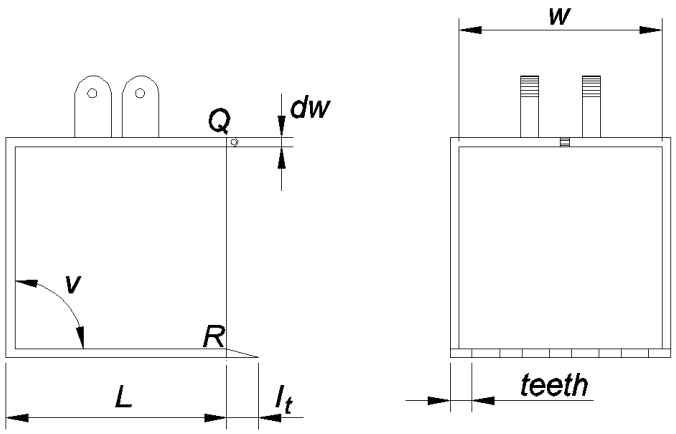

(a)

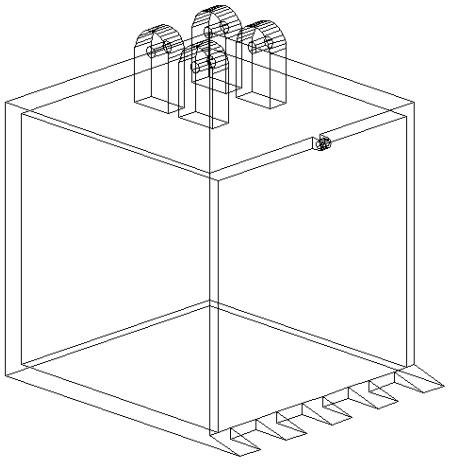

(b)

Fig. 13 Geometrical features of the shovel's dipper in the considered example application: (a) side view of the dipper (left sketch) and top view of the dipper (right sketch) and (b) isometric view of the dipper

Based on the simulated crowd and rope speeds shown in Fig. 14(a) and the initial values of the relevant parameters, the trajectory of the bucket tip with a maximum cutting depth of approximately *1.87 m* is presented in Fig. 14(b). It is worth noting that the simulated trajectory of the dipper has stopped when the payload weight attained its maximum and steady-state value of 177 kN

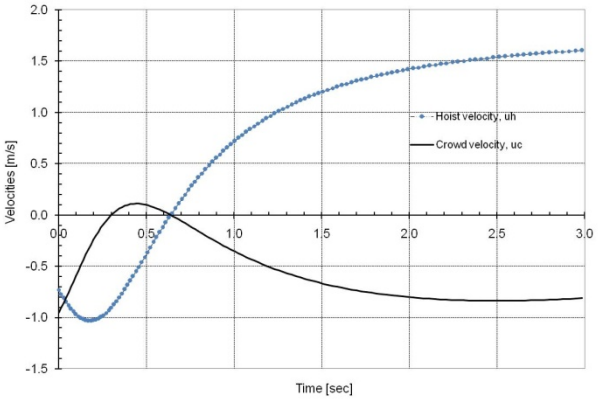

(a)

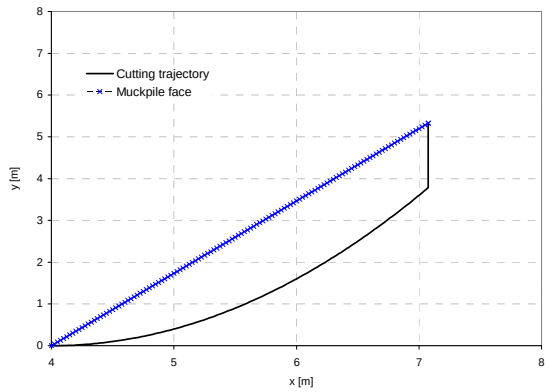

(b)

Fig. 14. (a) Prescribed hoist and crowd velocities and (b) trajectory of the dipper's tip

Fig. 15 displays the variation of the dipper's resistance forces with time for the considered dipper's trajectory shown in Fig. 14(b). It may be observed from this figure: (i) that the total cutting force is almost solely undertaken by the teeth of the bucket for indentation and excavation (continuous line in the graph), rather than by the side plates, and (ii) the payload weight becomes equal to the total cutting resistance force close to the end of the cycle of the digging process (i.e., in 2.1 sec) and then becomes larger than the former. This was expected since the current sizes of the shovels lead inevitably to significant payload resistance force compared to the cutting force. It is worth noting from this simulation that the payload weight reaches a steady state of 177 kN

before the programmed full cycle of digging operation (i.e., until the trajectory intersect the muckpile face in Fig. 14(b)). This shows that there is ample room for digging optimization that can be further explored.

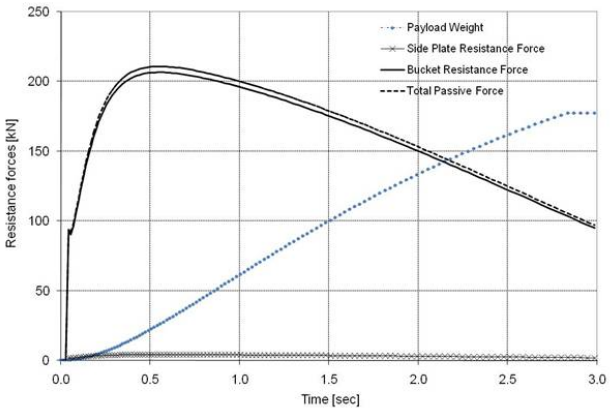

Fig. 15 Evolution with time of the payload weight F_1, as well as of the total cutting resistance force F_4 for the side plates, bucket tip separately, and total for the case at hand

Fig. 16 shows the evolution with time of the horizontal and vertical components, of the total cutting force undertaken by the teeth of the dipper. It is worth observing that the absolute value of the horizontal component of the cutting force is always larger than the absolute value of the vertical component despite the upwards motion of the dipper.

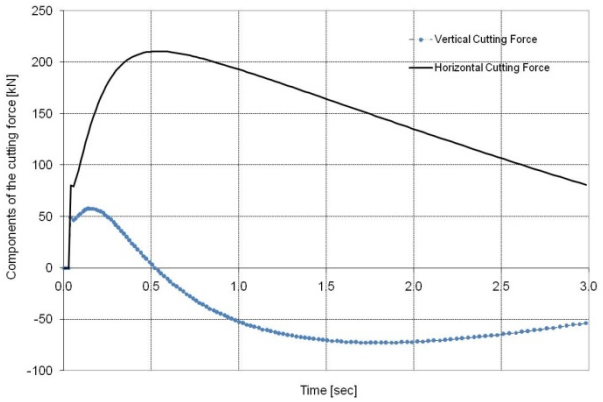

Fig. 16 Variation of horizontal and vertical components of the total cutting resisting force with time for the case at hand

Fig. 17 displays the evolution of the crowd and hoist specific energies, as well as the specific energy of cutting w.r.t. time along the digging-loading cycle for the problem at hand. It is seen from this figure that the specific energy of the hoist outweighs that of the crowd along the entire digging-loading cycle and this may be attributed to the fact that in the considered example the crowd velocity is always lower than the hoist speed. Also, it may be noted that after an initial phase in which the hoist motor specific energy is larger than that consumed in cutting, there is a second following phase in which both hoist and cutting specific energies attain comparable values.

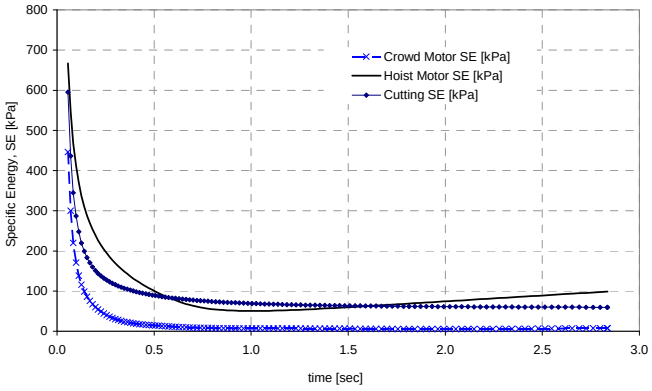

Fig. 17 Evolution of hoist motor, crowd motor and cutting specific energies with time

Furthermore, Fig. 18 illustrates the variation of the cutting specific energy SE_c of the shovel along its whole digging cycle with cutting depth. The specific energy of cutting can be rewritten in the following manner

$$SE_c = \frac{F_s}{\delta \cdot S} \tag{24}$$

in which F_s, δ, S denote the tangential cutting force, the penetration depth and the width of the cutting tool that is constant. The cutting force in a first approximation may be assumed to vary linearly with the penetration depth (Stavropoulou 2006), that is

$$F_s \approx a + b\delta + o(\delta^2) \tag{25}$$

where a is the intercept of the cutting force vs. penetration depth and b is the slope of the linear function. From the above formulae (24) and (25) it is derived

$$SE = \frac{F_s}{\delta \cdot S} = \frac{(a/S)}{\delta} + \left(\frac{b}{S}\right) \tag{26}$$

It is obvious from the above relationship that SE exhibits a (-1) power of the penetration depth size effect and the intrinsic SE is given by the term b/S. This simple model was then verified by best-fitting Eq. (26) on the data of the considered example case, as is illustrated in Fig. 18. From this analysis it was found that $b/S = 39\ kPa$ and $a = 29\ kPa \cdot m$.

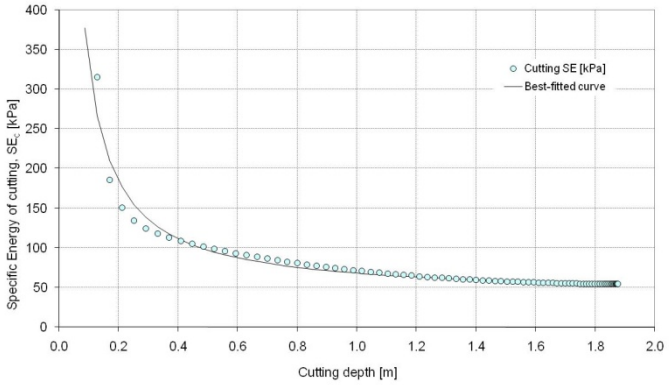

Fig. 18 Variation of the cutting specific energy of the cable shovel with the cutting depth along its excavation-loading cycle

6. Conclusions

A simplified – albeit analytical – model and algorithm have been presented for the fast calculation of forces exerted on a shovel dipper and specific energy of the cutting process. This algorithm has been implemented into an Excel™ spreadsheet to assist site engineers for shovel operation optimization or to facilitate the fast analysis of real-time monitoring data of shovel crowd and hoist motors. It requires no code to be written and is user friendly. The calculation of the cutting force is based on a plane strain logsandwich kinematical mechanism and the Upper-Bound theorem of Limit Analysis Theory. This failure mechanism was independently found from a LEFM analysis of a mixed-mode crack propagation along the soil bank due to passive loading of the latter. Also, the specific energies consumed by the crowd and hoist motors, as well as by the cutting process itself have been calculated. The specific energy of cutting exhibits a size effect, such that it decreases as the (-1)-power of the cutting depth for the considered example application. More cases could be analyzed with the proposed algorithm, but this is out of the scope of this paper.

References

Awuah-Offei, K. and Frimpong, S. (2007), "Cable shovel digging optimization for energy efficiency", *Mech. Mach. Theory*, **42**(8), 995-1006.

Awuah-Offei, K. and Frimpong, S. (2011), "Efficient cable shovel excavation in surface mines", *Geotech. Geol. Eng*., **29**(1), 19-26.

Blouin, S., Hemami, A. and Lipsett, M. (2001), "Review of resistive force models for earthmoving processes", *J. Aerospace Eng*., **14**(3), 102-111.

Chen, W.F. (1975), *Limit analysis and soil plasticity*, Elsevier Scientific Publishing Company, Amsterdam.

Detournay, E. and Atkinson, C. (2000), "Influence of pore pressure on the drilling response in low-permeability shear-dilatant rocks", *Int. J. Rock Mech. Min*., **37**(7), 1091-1101.

Exadaktylos, G. and Xiroudakis, G. (2009), "A G2 constant displacement discontinuity element for analysis, of crack problems", *Comput Mech*, **45**(4), 245-261.

Exadaktylos, G. and Xiroudakis, G. (2010a), "The G2 constant displacement discontinuity method. - Part I: Solution of plane crack problems", *Int. J. Solids Struct*., **47**(18-19), 2568-2577.

Exadaktylos, G. and Xiroudakis, G. (2010b), "The G2 constant displacement discontinuity method - Part II: Solution of half-plane crack problems", *Int. J. Solids Structures,* **47**(18-19), 2578-2590.

Frimpong, S. and Hu, Y. (2004), "Parametric Simulation of Shovel–Oil Sands Interactions During Excavation", *Int. J. of Surface Mining, Reclamation and Environment,* **18**(3), 205–219.

Hadjigeorgiou, J. and Scoble M.J. (1988), "Prediction of digging performance in mining", *Int. J. Surface Mining*, **2**(4), 237-244

Hemami, A., Goulet, S. and Aubertin, M. (1994), "Resistance of particulate media excavation: application to bucket loading", *Int. J. Surface Mining*, **8**(3),125-129.

Hendricks, C. and Scoble, M. (1990), "Post-blast evaluation through shovel performance monitoring", *Proceedings of the Conference on Explosive and Blasting Technique*, Canada Centre for Mineral and Energy Technology, 227–243.

Hustrulid, W. and Kuchta, M. (1995), *Open Pit Mine Planning and Design*, A.A. Balkema: Rotterdam.

Karpuz, C., Ceylanoglu, A. and Pasamehmetoglu, A.G. (1992), "An investigation on the influence of depth of cut and blasting on shovel digging performance", *Int. J. Surface Mining* , **6**(4), 161-167.

Lipsett, M.G. and Moghaddam, R.Y. (2011), *Modeling excavator-soil interaction*, Bifurcations, Instabilities and Degradations in Geomaterials, Springer Series in Geomechanics and Geoengineering, 347-366.

Maciejewski, J. and Jarzebowski, A. (2002), "Laboratory optimization of the soil digging process", *J. Terramechanics*, **39**(3), 161-179.

Palmer, A.C. and Rice, J.R. (1973), "The growth of slip surfaces in the progressive failure of over-consolidated clay", *Proc. Roy. Soc. Lond.* A., **332**, 527-548.

Paraszczak, J., Planeta, S. and Szymanski, J. (2000), "Performance and efficiency measures for mining equipment", MPES 2000: *Proceedings of the 9th Int. Symp. on Mine Planning and Equipment Selection*, Athens, Greece, 6-9 November.

Parker, A.P. (1981), *The Mechanics of Fracture and Fatigue: An Introduction*, E. & F. Spon in association with Methuen, Inc., New York.

Shi, N. and Joseph, T.G. (2006), "A new Canadian shovel dipper design for improved performance", *CIM Bulletin*, **99**, Volume 1 No. 2, March/April 2006, 6 pages.

Stavropoulou, M. (2006), "Modeling of small-diameter rotary drilling tests on marbles", *Int. J. Rock Mech. Min*., **43**(7), 1034-1051.